Application of the Woods-Saxon potential in studying quadrupole and octupole excited states using machine learning[*]

Hadi Sobhani[†]   Yan-An Luo

School of Physics, Nankai University, Tianjin 300071, People's Republic of China

Abstract: In this study, the energy bands of quadrupole and octupole excited states are investigated. This is achieved by employing the Bohr Hamiltonian, incorporating quadrupole and octupole deformations whose variables are accurately separated. Subsequently, the Woods-Saxon potential is added to the problem. Given that this problem cannot yield suitable solutions using conventional approximations, we solve it numerically using machine learning. A detailed description is given of how wave functions and their associated energies are obtained. It is demonstrated throughout this procedure how machine learning helps us and makes it easier to accomplish our objective. We have examined and analyzed the energy spectrum and possible multipole transitions for candidate isotopes ^{226}Ra and ^{226}Th.

Keywords: quadrupole and octupole excited states, Bohr Hamiltonian, Woods-Saxon potential, Machine learning method

DOI: **CSTR:**

I. INTRODUCTION

The study of protons and neutrons is the primary focus of atomic physics, which studies nucleons and their constituent parts. Nuclear deformation is one of the most thoroughly researched topics in which the non-spherical shape of a nucleus is described by quadrupole and octupole moments. Nuclear dynamics and organization are known to be significantly impacted by such deformation. The study of quadrupole [1] and octupole [2−4] deformations in nuclei has advanced recently, especially in cases when these two anharmonic forms interact. Nonuniform spatial charge distributions are the driving force behind this interaction, and deformations affect nuclear characteristics including energy levels and electromagnetic moments. To investigate the collective dynamics of nuclei, several models have been presented [5−8] (such as those with Davidson potentials and the analytical quadrupole-octupole axially symmetric model enclosed in an infinite well potential). Alternative possibilities are still being investigated, even though these models have drawbacks and don't always perform better than others.

Quadrupole deformations have long been linked to nuclear rotational spectra, and octupole deformations, or pear-shaped nuclei, are known to happen in some places, most notably among light actinides. A negative-parity band with levels $L^\pi = 1^-, 3^-, 5^-, \ldots$, etc. that are near in energy to the ground-state band and form a single band with $L^\pi = 0^+, 1^-, 2^+, 3^-, 4^+, \ldots$, etc. is one of the characteristics of octupole deformation [1]. Octupole vibrations are indicated by a negative-parity band that is higher than the ground-state band. Numerous authors have examined the shift from octupole vibrations to octupole deformation [9−11]. Although it has movable parameters, the sp-df-interacting boson model (IBM) [12, 13] is a comprehensive algebraic classification of states in the presence of both quadrupole and octupole degrees of freedom.

According to a recent review [14] and its references, machine learning (ML) has been combined with statistical techniques in the past ten years to address a range of nuclear physics problems, ranging from fundamental particles to the behavior of dense celestial bodies. A few of the applications concentrate on teaching machine learning models to predict nuclear observables directly, including fission yields [25], nuclear masses [15−19], charge radii [20−22], and beta-decay half-lives [23, 24]. Other applications of ML seek to enhance nuclear many-body simulations by using ML models to replace computationally intensive procedures. For example, collective Hamiltonians for low-lying nuclear states have been refined using deep neural networks [26], and density profiles for nuclear radii and binding energies calculations using density functional theory have been determined using back-propagation neural networks [27] and kernel

Ridge regression [28].

One of the most well-known potentials in nuclear physics is the Woods-Saxon potential [29]. This potential has deep roots in nuclear physics studies. However, this potential presents a significant challenge: the lack of an appropriate analytical solution. In other words, there is no exact analytical solution for such a potential for general angular momentum. One way to address this issue is to use the Pekeris approximation, but this approach leads to solutions involving Jacobi polynomials. Due to the limitations on the arguments of Jacobi polynomials, it is not possible to use these solutions for our purposes and multiple bands [30]. However, the aforementioned problem can be resolved using a different method, which we will discuss in detail later in the paper.

Our goal in this paper is to use the Woods-Saxon potential to investigate excited states resulting from quadrupole and octupole deformations. We aim to investigate the nuclei ^{226}Ra and ^{226}Th by considering the Woods-Saxon potential in a Hamiltonian that includes quadrupole and octupole deformations. Additionally, the optimization process required to reproduce experimental data relies on optimization algorithms, for which we will employ machine learning techniques. Furthermore, the steps for obtaining eigenvalues and eigenvectors will be implemented using a numerical approach. Therefore, we have organized the paper as follows: In Section 2, the theoretical foundations necessary for investigating such states are presented. To reproduce the experimental data, which is the subject of Section 3, we first examine the foundations of numerical calculations based on machine learning algorithms, and then proceed to reproduce experimental data, including the excitation spectrum and multipole transitions.

II. THE ANALYTIC QUADRUPOLE-OCTUPOLE AXIALLY SYMMETRIC MODEL

Two basic assumptions underlie the analytic quadrupole-octupole axially symmetric model [5, 6]. First, the axes of the quadrupole and octupole deformations are expected to align. In other words, the γ degree of freedom is ignored, but axial symmetry is assumed. Moreover, because they occur at extremely high energy levels, levels with none zero K (where K represents the projection of angular momentum along the body-fixed z-axis) are excluded [31]. On the other hand, this simplification makes the system easier to analyze. Thus, the form of the corresponding Hamiltonian is [31, 32]

$$H = -\sum_{\lambda=2,3} \frac{\hbar^2}{2B_\lambda} \frac{1}{\beta_\lambda^3} \frac{\partial}{\partial \beta_\lambda} \beta_\lambda^3 \frac{\partial}{\partial \beta_\lambda} + \frac{\hbar^2 \hat{L}^2}{6(B_2\beta_2^2 + 2B_3\beta_3^2)} + V(\beta_2, \beta_3), \tag{1}$$

where the quadrupole and octupole deformations are denoted by β_2 and β_3, respectively. The related masses that are connected to these distortions are B_2 and B_3. In the intrinsic reference frame, $\hat{L}$ is the angular momentum operator.

The following consideration can be used to find the answers to the Schrödinger equation [32]

$$\Phi_L^\pm(\beta_2, \beta_3, \theta) = (\beta_2\beta_3)^{-3/2} \Psi_L^\pm(\beta_2, \beta_3)|LM0, \pm\rangle, \tag{2}$$

where the set of Euler angles, θ, is necessary to understand and illustrate how the body-fixed coordinate system, defined by the axes x', y', and z', is oriented concerning the fixed laboratory coordinate system, defined by the axes $x, y,$, and z. This model uses the mathematical expression $|LM0, \pm\rangle$ to illustrate the rotation associated with an axially symmetric nucleus, focusing on the angular momentum projection M along the laboratory-fixed z axis and maintaining a projection K equal to 0 along the body-fixed z' axis [1]. The explicit form of the functions $|LM0, +\rangle$ and $|LM0, -\rangle$ are provided in [1, 5]. These functions transform in accordance with the irreducible representations (irreps) A and B_1 of the group D_2, respectively [31, 32].

$$|LM0, \pm\rangle = \sqrt{\frac{2L+1}{32\pi^2}}(1 \pm (-1)^L)\mathcal{D}_{0,M}^L(\theta) \tag{3}$$

in which Wigner functions of Euler angles are represented by $\mathcal{D}(\theta)$. The + label indicates positive parity states with $L = 0, 2, 4, \ldots$, whereas the $-$ label denotes those with $L = 1, 3, 5, \ldots$.

It is possible to simplify the Schrödinger equation by taking into account new deformation variables.

$$\tilde{\beta}_2 = \beta_2 \sqrt{\frac{B_2}{B}}, \qquad \tilde{\beta}_3 = \beta_3 \sqrt{\frac{B_3}{B}}, \qquad B = \frac{B_2 + B_3}{2}, \tag{4}$$

the polar coordinates in the range of $0 \le \tilde{\beta} < \infty$ and $-\pi/2 \le \phi \le \pi/2$ with the goal of the new deformation variables

$$\tilde{\beta}_2 = \tilde{\beta}\cos\phi, \qquad \tilde{\beta}_3 = \tilde{\beta}\sin\phi, \qquad \tilde{\beta} = \sqrt{\tilde{\beta}_2^2 + \tilde{\beta}_3^2}, \tag{5}$$

with the reduced energy $\epsilon = (2B/\hbar^2)E$, and the reduced potential $u = (2B/\hbar^2)V$. Then we have

$$\left[-\frac{\partial^2}{\partial \tilde{\beta}^2} - \frac{1}{\tilde{\beta}} \frac{\partial}{\partial \tilde{\beta}} + \frac{L(L+1)}{3\tilde{\beta}^2(1 + \sin^2\phi)} - \frac{1}{\tilde{\beta}^2} \frac{\partial^2}{\partial \phi^2} \right.$$
$$\left. + u(\tilde{\beta}, \phi) + \frac{3}{\tilde{\beta}^2 \sin^2 2\phi} - \epsilon_L \right] \Psi_L^\pm(\tilde{\beta}, \phi) = 0 \tag{6}$$

As a simplification, let us assume that the potential energy $u(\tilde{\beta},\phi)$ can be separated into the form $u(\tilde{\beta},\phi) = u(\tilde{\beta}) + u(\phi)/\tilde{\beta}^2$: a function of only, $u(\tilde{\beta})$, and a function of ϕ. Such a hypothesis permits us to separate Eq. (6) into two independent equations. We further assume that $u(\phi)$ is a very steep, double-well potential centered around $\pm\phi_0$. Then we have

$$\tilde{\beta}^2 \left[-\frac{d^2}{d\tilde{\beta}^2} - \frac{1}{\tilde{\beta}}\frac{d}{d\tilde{\beta}} + u(\tilde{\beta}) - \epsilon_{\tilde{\beta}}(L) \right] \psi_L^\pm(\tilde{\beta}) = -\varrho^2 \psi_L^\pm(\tilde{\beta}), \quad (7)$$

and

$$\left[\frac{d^2}{d\phi^2} - u(\phi) - u_L(\phi) \right] \chi^\pm(\phi) = -\varrho^2 \chi^\pm(\phi), \quad (8)$$

$$u_L(\phi) = \frac{L(L+1)}{3(1 + \sin^2\phi)} + \frac{3}{\sin^2 2\phi} \quad (9)$$

where the total wave function has been assumed as $\Psi_L^\pm(\tilde{\beta},\phi) = \psi_L(\tilde{\beta})\chi_L^\pm(\phi)$, the separation constant ϱ^2. Hereafter, for the sack of simplicity, the $\pm$ will be omitted. There is an important, exciting a periodic term, $u_L(\phi)$. It will impact the later calculation of the electromagnetic transitions.

Equation (8) contains the function $u_L(\phi)$ in this separation process. It is obvious that having a term like that in the equation makes it much more difficult to solve and analyze. Given that it is a well-defined, smooth, and differentiable function, this problem can be solved by applying the Taylor expansion of this function around its minimum value, as described in [33]. Consequently, we have:

$$u_L(\phi) \approx u_L(\phi_L) + \frac{u''(\phi_L)}{2}(\phi - \phi_L)^2, \quad (10)$$

where, for a given L, ϕ_L is the minimum of $u_L(\phi)$. It is worth noting that since $u_L(\phi)$ attains its minimum value at ϕ_L, the first derivative of $u_L(\phi)$ at ϕ_L will be zero. Consequently, the first derivative does not appear in the Taylor expansion for this reason. To transform the differential equation into the familiar form of the harmonic oscillator differential equation, we must not only substitute the Taylor expansion into the differential equation (8), but also, as outlined in [33], neglect the potential $u(\phi)$. Thus, we have:

$$-\frac{d^2\chi}{d\zeta^2} + \zeta^2\chi = \varepsilon_L\chi, \quad (11)$$

which introduces the following new parameters:

$$\zeta_L^2(\phi) = \sqrt{\frac{u_L''(\phi_L)}{2}}(\phi - \phi_L)^2, \quad \varepsilon_L = \frac{v^2 - u_L(\phi_L)}{\sqrt{\frac{u_L''(\phi_L)}{2}}}. \quad (12)$$

This differential equation has eigenvalues given by $\varepsilon_L = 2n + 1$, where n is the oscillation quantum number. Therefor we may have

$$\varrho^2 = \varrho_L^2 = \sqrt{\frac{u_L''(\phi_L)}{2}}(2n+1) + u_L(\phi_L). \quad (13)$$

Additionally, it should be noted that, moving forward, we will restrict our analysis to the case $n = 0$. We emphasize here that the parameter ρ is dependent on the angular momentum, ρ_L. This dependence is evident in our calculations of electromagnetic transitions. This is because that this parameter appeasers in the eigen function of the ϕ part

$$\chi_{n_\phi,L}(\phi) = N_{n_\phi,L} \exp\left(-\frac{\zeta_L^2(\phi)}{2}\right) H_{n_\phi}\left(\zeta_L^2(\phi)\right), \quad (14)$$

where $N_{n_\phi,L}$ is the normalization constant, and Hermit polynomials are shown by H_{n_ϕ}. If the Hermite and polynomial functions' arguments were independent of angular momentum, the normalization constant could end up simplified to a function of n_ϕ. Unfortunately, this is not the case in our case. The angular momentum dependence adds difficulties that prevent us from obtaining an analytical solution for the normalizing constant. However, numerical calculation can be easily used to calculate its value

$$N_{n_\phi,L} = \left[\int_{-\pi/2}^{\pi/2} \left| \chi_{n_\phi,L}(\phi) \right|^2 d\phi \right]^{-1/2}. \quad (15)$$

Now that the separation parameter has been determined based on the problem's known information, we can analyze the beta part of the differential equation.

It is now appropriate to present the potential that we are interested in: the Woods-Saxon potential. [1, 29, 30]

$$u(\tilde{\beta}) = \frac{-U_0}{1 + e^{a(\tilde{\beta}-\tilde{\beta}_0)}} \quad (16)$$

where the non-negative parameters U_0, a, and $\tilde{\beta}_0$ are present. This potential makes it clear that it lacks a hard-core, and its shape simplifies to a square well potential in the limit of $a \to \infty$. The Schrödinger equation including such potential cannot be solved correctly and analytically, even though it satisfies physical predictions well. This is another significant mathematical point regarding this potential [30]. Naturally, approximations like the Pekeris approximation have been used to present analytical solu-

tions for this purpose. However, the final answer contains Jacobi polynomials, and those polynomials impose restrictions on their parameters. Upon numerical evaluation of the physical constants, we will find that these restrictions are not satisfied, and practically, we are unable to extract appropriate experimental data from those analytical solutions. Stated differently, we are only able to address a limited amount of the experimental data using those answers. This is because the system in question cannot be sufficiently described by such mathematical approximations.

We employ an alternative approach to obtain the solution of the differential equation (7) in the presence of the Woods-Saxon potential (16). This method has been applied to a number of problems. The problem of single-particle levels in deformed nuclei is among the most significant of them [34−36]. In essence, we want to use this method to estimate the solution to a specific degree of precision. We start by assuming appropriate the bases functions in order to accomplish this. We indicate whole sets of functions that allow us to fully expand a function by using the proper base functions. We may save only a few chosen terms of this infinite expansion, as the name approximation implies. This is achieved when the results no longer differ significantly for a certain number of terms considered in the expansion. Therefore, we must start by adopting suitable basic functions. A strong basis is one that can accurately characterize the system's states across the same domain. The harmonic oscillator the basis provided by is among the most often used bases.

$$g_{\nu,n_\phi,L}(\tilde{\beta}) = \sqrt{\frac{2\nu!}{\Gamma(\nu + \varrho + 1)}} \tilde{\beta}^\varrho e^{-\tilde{\beta}^2/2} \mathscr{L}_\nu^\varrho(\tilde{\beta}^2), \qquad (17)$$

where the number of nodes in the $\tilde{\beta}$ direction is indicated by ν in this equation. Γ represents the gamma function, a known special function, and $\mathscr{L}$ displays the corresponding laguerre polynomials. By solving Eq. (7) for a system with the potential $u(\tilde{\beta}) = \tilde{\beta}^2$, this particular basis set can be directly obtained.

Actually, we can get the answer as follows by applying this principle. [37]:

$$\psi_{n,L}(\tilde{\beta}) = \sum_\nu C_{\nu,L}^{a,\tilde{\beta}_0,U_0} g_{\nu,L}(\tilde{\beta}), \qquad \sum_\nu \left(C_{\nu,L}^{a,\tilde{\beta}_0,U_0}\right)^2 = 1, \quad (18)$$

It is clear that the numerical values of the free parameters in the differential equation (7) have a substantial impact on the coefficients $C_{\nu,L}^{a,\tilde{\beta}_0,U_0}$. Essentially, for any distinct state of Eq. (7), we will have an appropriate linear combination of the harmonic oscillator basis functions. The matrix eigenvalue problem is solved to get the coefficients of this expansion, and the elements are computed as follows:

$$\langle \nu' | \hat{H}_{\tilde{\beta}} | \nu \rangle \equiv \int_0^\infty \tilde{\beta} \mathrm{d}\tilde{\beta} \, g_{\nu'L}(\tilde{\beta}) \hat{H}_{\tilde{\beta}} g_{\nu L}(\tilde{\beta}), \qquad (19)$$

$$\hat{H}_{\tilde{\beta}} = -\frac{\mathrm{d}^2}{\mathrm{d}\tilde{\beta}^2} - \frac{1}{\tilde{\beta}}\frac{\mathrm{d}}{\mathrm{d}\tilde{\beta}} + \frac{\varrho_L^2}{\tilde{\beta}^2} - \frac{U_0}{1 + e^{a(\tilde{\beta} - \tilde{\beta}_0)}} \qquad (20)$$

as one knows

$$\hat{H}_{\tilde{\beta}} | n, L; \phi_L; a, \tilde{\beta}_0, U_0 \rangle = \epsilon_{\tilde{\beta}} | n, L; \phi_L; a, \tilde{\beta}_0, U_0 \rangle. \qquad (21)$$

The following is a description of the methods used to address this issue: The matrix elements, as expressed in equation (19), must be calculated for each quantized angular momentum inside each nucleus. Then by solving the eigenvalue problem, one may obtain the relevant eigenvalues and eigenvectors, which in turn can be used to determine the energy levels of states with different numbers of nodes according to the given angular momentum. The way the solution's numerical precision is taken into consideration is another important aspect of this. The number of terms taken into account in the expansion (18) has a direct correlation with accuracy. It is easy to see that the results converge to a certain value when more terms are added to this expansion. The degree of precision needed to solve the problem determines the degree of convergence. As a result, we estimate 10 terms in this expansion based on the facts taken into consideration in this study. This number of terms gives our answer a level of precision that is sufficient. On the other hand, finding the ideal values for the free parameters is necessary for this process. Although the factors involved in this methodology will be explained in the next part, the observations of this segment are summarized in the appendix, the specifics of which are left for the section on numerical calculations.

The experimental results can now be reproduced by numerical computations. In the part that follows, this will be discussed.

III. NUMERICAL RESULTS

In this section, we aim to reproduce the experimental data of some nuclei using the information gathered in the previous section. As mentioned in the introduction, machine learning techniques form the basis of the computational investigations in this work. Specifically, our goal is to use a machine learning optimization technique to find the optimal values for the problem-relevant free parameters so that we can reproduce the experimental results. Gradient descent [39], an algorithm for determining a function's minimum value that is frequently used to lower errors in prediction models, is one of the most significant optimization strategies in machine learning. Gradient descent reduces the difference between the model's predic-

tions and the real empirical data (i.e., the loss function or the deviation function) by progressively changing the parameters during the model's training phase.

Gradient descent systematically refines the model parameters from an initial approximation by moving toward error minimization. According to [39], if we gather all of the parameters that affect the deviation function or the loss function in a vector notation $\boldsymbol{\vartheta} = (\vartheta_1, \vartheta_2, \dots)$, they are revised after each iteration

$$\boldsymbol{\vartheta} \rightarrow \boldsymbol{\vartheta} - \eta \cdot \nabla\sigma, \tag{22}$$

where σ is the deviation function defined in accordance with our objective and η is the learning rate.

$$\sigma = \sqrt{\frac{1}{N}\left(\frac{E_{\exp}(L_i^\pi)}{E_{\exp}(2^+)} - \frac{E_{\text{theo}}(L_i^\pi) - E_{\text{theo}}(0^+)}{E_{\text{theo}}(2^+) - E_{\text{theo}}(0^+)}\right)^2}, \qquad \pi = \pm, \tag{23}$$

where N is the number of data used for each isotope, and $E_{\exp}$ (from Ref. [38]) and E_{theo} stand for the experimental and theoretical energies, respectively. By determining how steeply the loss function changes in relation to each parameter, it shows the slope or rate of adjustment. The method basically "descends" towards a minimum error threshold by traveling in the opposite direction of the gradient in order to arrive at an optimal or nearly optimal solution.[39] Unlike instructional resources like [39], textbook optimization tasks usually employ a simple mathematical function. But the function we are trying to improve is not a mathematical function and does not have a continuous domain. This is due to the fact that in order to retrieve the energies, the matrix of each angular momentum in (19) must be found first, and then the pertinent energies must be calculated using diagonalization. Consequently, the optimization technique needs to incorporate district theoretical data.

A. Energy spectrum

After describing the fundamental computations in the previous section, we now go on to the findings. Only the isotopes of ^{226}Ra and ^{226}Th are examined in this article. Table 1 displays the values that were acquired during the optimization procedure for every isotope. Each row in the table corresponds to a distinct isotope since the isotopes are identified in the table. The number of digits in free parameters to the right of the decimal point is a highly

special feature of the machine learning approach. In other words, using more basic approaches, such as search algorithms, to obtain free parameters with such accuracy would have required time that cannot be quantified in normal units of time to accomplish the level of accuracy offered in the preceding equations. The last column also states the σ parameter for each isotope.

The appendix to this paper provides a summary of the outcomes obtained using these values. These tables display the state's angular momentum value in the first column, the experimental normalized energy value in the second, the theoretical normalized energy in the third, and the coefficients in the wave function expansion in the remaining columns. These tables are organized according to the isotopes covered in this work, and it is reasonably simple to locate the information required for each isotope and angular momenta value in each of them. Note that only the level of $n_{\tilde{\beta}} = 0$, and hence $n_\phi = 0$, has been included in the energy level computations. Therefore, in the subsequent discussions, these will not be included when using the aforementioned numbers as indices.

Plotting the potential that produced the best fit for each isotope will be the first step in analyzing the study's findings. Figure 1 was drawn using the information in Table 1 and equation (16). Each isotope's potential is shown in a different color in this picture. An interesting pattern is seen: the potential shape shifts from the well-known Woods-Saxon form to a finite well as the mass number increases. The reason for this behavior is because as the
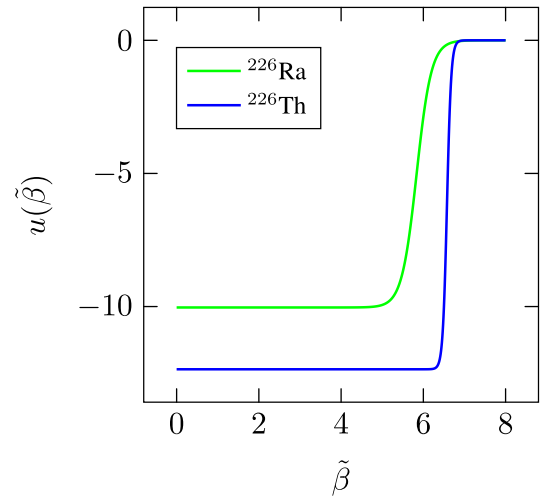
Fig. 1. (color online) A visualization of the potential energy shape for each isotope after optimizing the parameters.

Table 1. Values of free parameters for each isotope.

Isotope	a	$\tilde{\beta}_0$	U_0	σ_{Ours}	$\sigma_{\text{Ref. [33]}}$
^{226}Ra	5.558247546040683	5.836410397132373	10.03477806863556	0.949	1.163
^{226}Th	19.654234566878788	6.574464293524817	12.356356546357798	0.942	1.093

optimization process progressed, the value of the parameter a increased.

The following step shows the experimental and expected spectra for the nuclei under consideration in Figure 2. The precision of the theoretical predictions in comparison to the experimental data is better shown in this picture. The graphical representations display the theoretical predictions in red and the experimental data in black. Additionally, to better compare excitation states with different parities, they are plotted separately. For better comparison and understanding of the discrepancy between the theoretical prediction and experimental data, these levels are connected by dotted lines. Naturally, the steeper the slope of these dotted lines, the greater the difference between them. Furthermore, we have shown the predictions from Ref. [33] (named as PFM) in green in this figure to offer a visual comparison between our calculations and that reference.

One noteworthy finding from this figure is that, in every instance, the trend of the experimental values in the positive parity band is correctly predicted. However, in the negative parity band, this tendency is a little different. The theoretical predicted is typically marginally lower than the experimental results for the lowest few levels of the negative parity band. This is because, as other investigations have shown, these levels need a little more energy to reproduce, which is not achievable with this Hamiltonian structure and potential [30].

Before beginning to calculate electromagnetic transitions, it is useful to examine the wave functions that have been computed for these isotopes. The ϕ part's wave functions were Hermite polynomial expressions, while the $\tilde{\beta}$ section's wave functions were obtained by using lin-

ear combinations of the basis functions given in Eq. (17). To illustrate their differences, we have included both the basis functions and the wave functions for ^{224}Ra in Figure 3. This figure consists of four panels. The upper panels show positive parity, while the lower panels show negative parity. The left panels display the wave functions as a function of $\tilde{\beta}$, and the right panels display the basis functions. The difference between the basis functions and the wave functions is evident. For instance, The wave and basis functions have different values at different places. To understand this, consider the size of the vertical axis.

B. B(EL) transition rates

The electric dipole, quadrupole, and octupole operators in the presence of axial symmetry are [31]

$$T_\mu^{(E1)} = t_1\beta_2\beta_3 \mathcal{D}_{\mu,0}^{(1)}(\theta) = t_1 \frac{B}{\sqrt{B_2 B_3}} \tilde{\beta}^2 \frac{\sin 2\phi}{2} \mathcal{D}_{0,\mu}^{(1)}(\theta),$$
(24a)

$$T_\mu^{(E2)} = t_2\beta_2 \mathcal{D}_{\mu,0}^{(2)}(\theta), = t_2 \sqrt{\frac{B}{B_2}} \tilde{\beta}\cos\phi \mathcal{D}_{0,\mu}^{(2)}(\theta),$$
(24b)

$$T_\mu^{(E3)} = t_3\beta_3 \mathcal{D}_{\mu,0}^{(3)}(\theta) = t_3 \sqrt{\frac{B}{B_3}} \tilde{\beta}\sin\phi \mathcal{D}_{0,\mu}^{(3)}(\theta),$$
(24c)

where t_1 is a constant and

$$t_2 = \frac{3Ze}{4\pi}R^2, \quad t_3 = \frac{3Ze}{4\pi}R^3, \quad R = (1.2)A^{1/3}.$$
(25)

Fig. 2. (color online) Comparison between predicted and experiments spectra of the considered nuclei and predictions of the parameter-free model [33] (PFM).
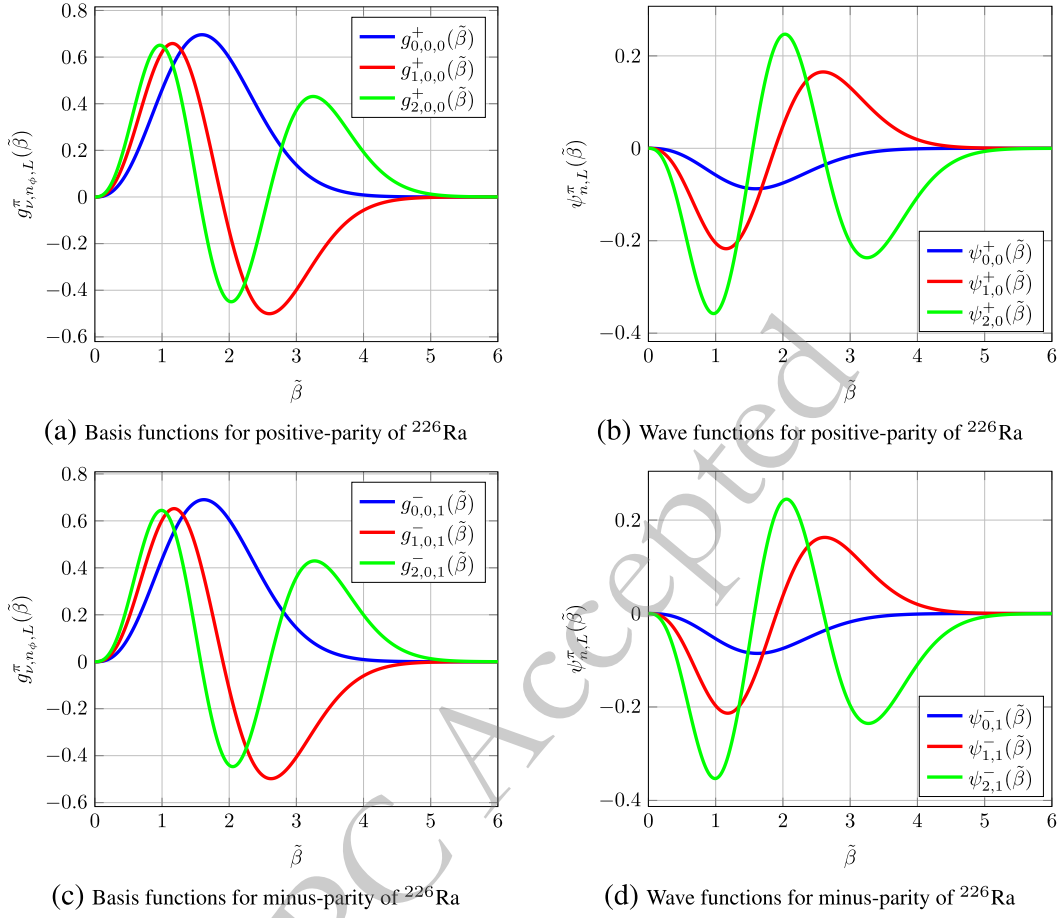
(a) Basis functions for positive-parity of ^{226}Ra

(b) Wave functions for positive-parity of ^{226}Ra

(c) Basis functions for minus-parity of ^{226}Ra

(d) Wave functions for minus-parity of ^{226}Ra

Fig. 3. (color online) Graphical comparison between the bases and actual wave function obtained as a linear combinations of basis functions.

Combining equations (3) and $\Psi_L^{\pm}(\tilde{\beta}, \phi)$ results in the final wave function. To get the transition rate B(EL) for this wave function, use the formula below:

$$B(\mathrm{EL}; L_i a_i \to L_f a_f) = \frac{\left| \left(L_f a_f \left\| T^{(\mathrm{EL})} \right\| L_i a_i \right) \right|^2}{2L_i + 1} \qquad (26)$$

in which Wigner-Eckart theorem [40] is applied to calculate the reduced matrix element.

$$\left\langle Lf\mu_f a_f \right| T^{(\mathrm{EL})} \left| L_i \mu_i a_i \right\rangle = \frac{(L_i L L_f | \mu_i \mu \mu_f)}{\sqrt{2L_f + 1}} \left(L_f a_f \left\| T^{\mathrm{EL}} \right\| L_i a_i \right) \qquad (27)$$

where $(L_i L L_f | \mu_i \mu \mu_f)$ stands for the Clebsch-Gordan coefficient.

In Eq. (26), the integration over angles θ uses a typical integral over three Wigner functions [40], yielding $(L_i L L_f | 000)$. The remaining integrations are carried out across $\iint \beta_2^3 \mathrm{d}\beta_2 \, \beta_3^3 \mathrm{d}\beta_3$, where the β_2^3 and β_3^3 factors come from the volume element. The integration is over $\int \tilde{\beta} \mathrm{d}\tilde{\beta} \mathrm{d}\phi$, up to constant factors, as per Eqs. (4) and (5) and the relevant Jacobian.

By examining the formulas in (24), we can see that the calculation of the electromagnetic transition can be decomposed into four factors. The first factor is a purely constant parameter that depends only on the fundamental properties of the isotope in question. However, the other three factors depend entirely on the initial and final state information and the transition order. Thus, the formula for calculating the electromagnetic transition can be written as follows [6]:

$$B(\mathrm{E}\lambda; L_i \to L_f) = C \left(I_{\tilde{\beta}}^{(\mathrm{E}\lambda)} \right)^2 \left(I_{\phi}^{(\mathrm{E}\lambda)} \right)^2 (L_i L L_f | 000)^2, \qquad (28)$$

where C is a constant and

$$I_{\tilde{\beta}}^{(\mathrm{E}2)} = I_{\tilde{\beta}}^{(\mathrm{E}3)} = \int \tilde{\beta}^2 \psi_{n_i, L_i} \psi_{n_f, L_f} \mathrm{d}\tilde{\beta}, \qquad (29)$$

$$I_{\tilde{\beta}}^{(\mathrm{E}1)} = \int \tilde{\beta}^3 \psi_{n_i, L_i} \psi_{n_f, L_f} \mathrm{d}\tilde{\beta}, \qquad (30)$$

$$I_{\phi}^{(\mathrm{E}1)} = \int_{-\frac{\pi}{2}}^{\frac{\pi}{2}} \sin 2\phi \chi_{n_{\phi_i}, L_i} \chi_{n_{\phi_f}, L_f} \, \mathrm{d}\phi, \qquad (31)$$

$$I_\phi^{(E2)} = \int_{-\frac{\pi}{2}}^{\frac{\pi}{2}} \cos\phi \, \chi_{n_{\phi_i},L_i} \chi_{n_{\phi_f},L_f} \, d\phi, \tag{32}$$

$$I_\phi^{(E3)} = \int_{-\frac{\pi}{2}}^{\frac{\pi}{2}} \sin\phi \, \chi_{n_{\phi_i},L_i} \chi_{n_{\phi_f},L_f} \, d\phi, \tag{33}$$

and at the end of this part of the article, we suggest readers to Ref. [6] for more valuable information on the integrals and equations.

Unfortunately, we were unable to find sufficient experimental data for electromagnetic transitions of the considered nuclei in reference [38]. However, a comparison of the trends obtained in this study would still be interesting and informative. If readers refer to the section on solving differential equations in this article, they will see that, unlike the case of approximate separation, electromagnetic transitions are influenced by both parts of the solution, namely $\tilde\beta$ and ϕ. In the case of approximate separation, since the ϕ part was merely a constant factor, it was automatically eliminated by calculating the ratio of electromagnetic transitions. However, this is no longer applicable here. Although we have limited ourselves to $n_\phi = 0$ and in the Hermite functions we have $H_0 = 1$, the normalization constant will be a function of the angular momentum value because the argument of the exponential function ζ^2 contains ϕ_L, and this value takes a specific value for each value of angular momentum. This is what causes the difference in the trend of theoretical predictions in the calculation of electromagnetic transitions in the present model.

To illustrate the trend of theoretical predictions of our model, we have plotted the calculated electromagnetic transitions in Figures 4, 5, and 6. In Figure 4, we have calculated the electromagnetic transitions $B(E1, L \rightarrow L-1)$ for the model [33] and our results, and finally normalized them to the value of $B(E1, 1^- \rightarrow 0^+)$. We believe that the authors of [33] used the same approximate separation [5] formulae of $B(EL)$ transitions because the values of their electromagnetic transitions were obtained in the same way. In this case, the theoretical prediction predicts an upward trend with increasing L, but this is not the case for the predictions made by the results of this article. If we look at this trend more closely, the theoretical predictions for the $B(E1)$ transition suggest an oscillatory trend, but overall this trend is upward. The change in this oscillatory trend is more significant and severe in ^{226}Th than in ^{226}Ra, while for the parameter-free model, the theoretical prediction trend for the $B(E1)$ transition is strictly upward.

For the $B(E2)$ electromagnetic transition, a behavior different from the parameter-free model is predicted. In this case, for transitions involving positive parity states, an initial increase in the transition value is predicted, followed by a decrease. On the other hand, for $B(E2)$ electromagnetic transitions involving negative parity states, an initial decrease is predicted followed by a relative growth. In contrast, the parameter-free model does not predict any decrease in $B(E2)$ transition values with increasing angular momentum. This is clearly illustrated in
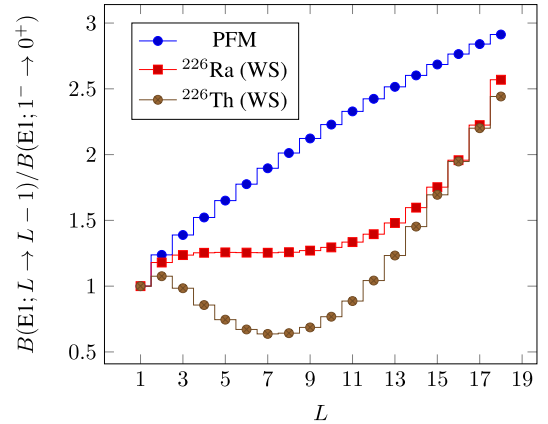

Fig. 4. (color online) Comparison of theoretical calculations of $B(E1)$ electromagnetic transitions in parameter-free and WS models
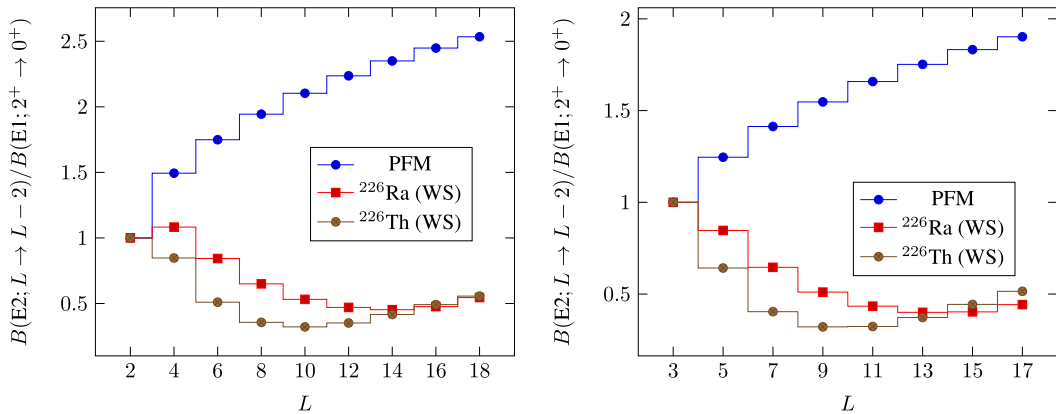

Fig. 5. (color online) The same as Figure 4, but for $B(E2)$ electromagnetic transitions. The left panel belongs to the positive-parity sates, while the right panel is for the minus-parity states.
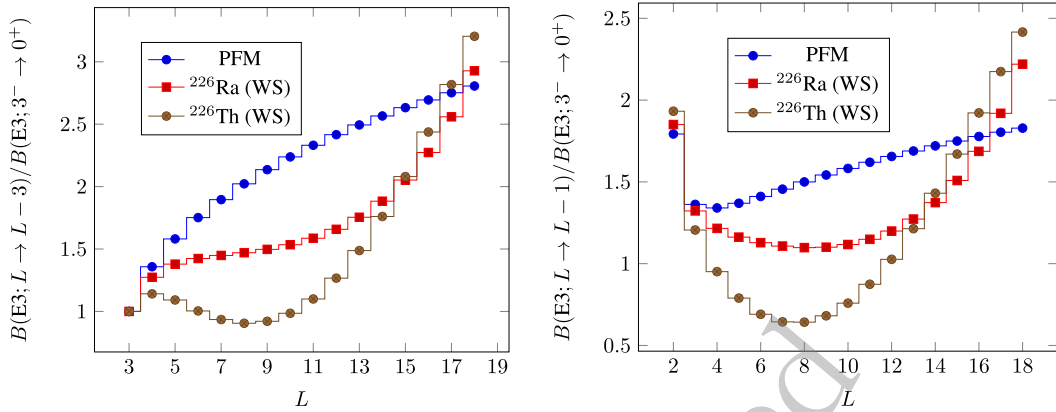
Fig. 6. (color online) The same as Figure 4, but for B(E3) electromagnetic transitions. The left panel shows transitions with a ΔL of three units between initial and final states, while the right panel shows transitions with a ΔL of one unit.

Figure 5. The transition values in this figure are normalized B(E2, $2^+ \rightarrow 0^+$). The left panel of this figure shows electromagnetic transitions involving states with positive parity, while the right panel corresponds to states with negative parity.

However, the predicted trends for B(E3) electromagnetic transitions in the parameter-free model and the model discussed in this paper are somewhat similar. We have examined these transitions in two different categories. All values considered in this figure are normalized to the B(E3; $3^- \rightarrow 0^+$) transition. This category includes transitions where the difference in angular momentum between the starting and ending states is three units. In the left panel of Figure 6, you can see the predicted behavior for these transitions. The figure shows that the model predicts an increasing trend for these transitions, and the slope becomes gentler as the angular momentum value goes up. However, in our calculations, although the overall behavior is upward, the rate of change is quite different. For ^{226}Ra, for angular momenta less than 15, the slope of this change is gentle, but for angular momenta greater than 15, the slope of this trend becomes steeply upward. In contrast, for ^{226}Th, in the angular momentum range of $4 \leq L_i \leq 9$, this trend experiences a relative decline, then either a steep upward slope.

The second category of B(E3) electromagnetic transitions is those with a one-unit difference between the initial and final states. The result of this investigation is shown in the right panel of Figure 6. The overall trend for all three cases is similar but not identical. In all three cases, the values of these transitions initially experience a decrease, and then this trend increases. This trend for the parameter-free model has a nearly uniform rate, while for our model, both the decreasing trend is more pronounced and the slope of the increasing values is steeper.

IV. CONCLUSION

In this study, we aimed to investigate the application of the Woods-Saxon potential to describe excited states arising from quadrupole and octupole deformations. To this end, we employed a numerical method to compute the eigenfunctions and eigenvalues of the Hamiltonian. This process was simultaneously coupled with a machine learning optimization algorithm to evaluate the optimal solutions. Subsequently, we proceeded with the analysis of the results. Energy levels with different parities for ^{226}Ra and ^{226}Th were examined using both this model and the parameter-free model. Afterwards, we proceeded to calculate electromagnetic transitions and discussed how the exact separation of variables in the model presented in this paper could affect the calculation of electromagnetic transition values. Electric dipole, quadrupole, and octupole transitions were extensively analyzed and visualized. We observed that the trend predicted by our model was significantly different from that predicted by the parameter-free model. The reason for this difference was investigated, and it was found that the angular part of the Hamiltonian becomes a function of angular momentum in the exact separation. This manifests itself in the overlap of wave functions during the calculation of electromagnetic transitions.

APPENDIX

The appendix contains a detailed list of each isotope's normalized energies and wave function expansions. For more information on how to understand this data, return to the main text of the article.

Table 2. Normalized energies and wave function coefficients expansion of ^{224}Ra.

L	Exp. [38]	Theo.	$v = 0$	$v = 1$	$v = 2$	$v = 3$	$v = 4$	$v = 5$	$v = 6$	$v = 7$	$v = 8$	$v = 9$
0	0.000	0.000	-0.3356183853	0.4601163135	-0.4897062874	0.4505819956	-0.3670331573	0.2617959960	-0.1562957389	0.0698176536	-0.0158171870	-0.0036560333
1	3.747	0.337	-0.3320798429	0.4588960446	-0.4906960185	0.4524808776	-0.3685330316	0.2621360470	-0.1554623931	0.0684309260	-0.0146942714	-0.0040865223
2	1.000	1.000	-0.3258283252	0.4567842794	-0.4925691799	0.4559291880	-0.3711134798	0.2624601534	-0.1535905963	0.0655267032	-0.0125342736	-0.0048592957
3	4.749	1.966	-0.3181701537	0.4543356854	-0.4951707502	0.4603620583	-0.3740962562	0.2622124328	-0.1503969407	0.0614196291	-0.0095288033	-0.0058106949
4	3.127	3.196	-0.3104089198	0.4521519106	-0.4983574091	0.4651875797	-0.3767783229	0.2608595358	-0.1456856596	0.0559497979	-0.0059731975	-0.0067370896
5	6.603	4.647	-0.3034832001	0.4507078368	-0.5020251254	0.4699358412	-0.3786183631	0.2580482922	-0.1394337654	0.0494828575	-0.0022099817	-0.0074480610
6	6.155	6.279	-0.2977828667	0.4502802754	-0.5061049946	0.4743048841	-0.3792904112	0.2536284057	-0.1317636229	0.0423417616	0.0014445236	-0.0078060662
7	9.264	8.063	-0.2937684445	0.4509789661	-0.5105450086	0.4781224346	-0.3786343987	0.2475922793	-0.1228755534	0.0348448023	0.0047389883	-0.0077356502
8	9.891	9.980	-0.2911225829	0.4528090055	-0.5152941648	0.4812886257	-0.3765869515	0.2400118015	-0.1130003916	0.0272794881	0.0074909379	-0.0072145040
9	12.677	12.017	-0.2898522236	0.4557199787	-0.5202944199	0.4837358483	-0.3731341605	0.2310003354	-0.1023777809	0.0198980530	0.0095777500	-0.0062611990
10	14.185	14.165	-0.2898416927	0.4596353243	-0.5254787416	0.4854080602	-0.3682873158	0.2206944582	-0.0912475785	0.0129188438	0.0109273192	-0.0049249123
11	16.743	16.418	-0.2909767098	0.4644682759	-0.5307723062	0.4862524582	-0.3620721758	0.2092454854	-0.0798454475	0.0065273832	0.0115110616	-0.0032772609
12	18.931	18.774	-0.2931540960	0.4701303256	-0.5360948090	0.4862169665	-0.3545246386	0.1968148841	-0.0683991739	0.0008762172	0.0113385347	-0.0014053723
13	21.388	21.227	-0.2962849584	0.4765356481	-0.5413627981	0.4852502783	-0.3456890948	0.1835710565	-0.0571249543	-0.0039158050	0.0104526333	0.0005943711
14	24.061	23.776	-0.3002949086	0.4836031641	-0.5464915222	0.4833027678	-0.3356178941	0.1696867046	-0.0462238274	-0.0077640914	0.0089247470	0.0026221047
15	26.536	26.419	-0.3051229136	0.4912571029	-0.5513961416	0.4803276121	-0.3243713360	0.1553366406	-0.0358785697	-0.0106182512	0.0068496610	0.0045797499
16	29.523	29.155	-0.3107194183	0.4994264887	-0.5559923535	0.4762820060	-0.3120180934	0.1406960933	-0.0262312452	-0.0124612649	0.0043402161	0.0063756938
17	32.126	31.982	-0.3170441321	0.5080439460	-0.5601966237	0.4711284630	-0.2986359878	0.1259394558	-0.0174814083	-0.0133078987	0.0015218372	0.0079288019
18	35.300	34.900	0.3240636677	-0.5170441108	0.5639262645	-0.4648363124	0.2843130580	-0.1112393430	0.0096848575	0.0132024602	0.0014729501	-0.0091717132
19	38.099	37.908	0.3317492415	-0.5263619768	0.5670995962	-0.4573833940	0.2691487135	-0.0967665947	0.0029527646	0.0122159930	0.0045099233	-0.0100533940
20	41.375	41.004	0.3400745900	-0.5359314254	0.5696363501	-0.4487579085	0.2532547646	-0.0826847141	-0.0026489130	0.0104429634	0.0074583951	-0.0105409236
21	44.412	44.189	0.3490142425	-0.5456841613	0.5714584266	-0.4389602818	0.2367560076	-0.0691573910	-0.0070798083	0.0079974640	0.0101961966	-0.0106204913
22	47.750	47.461	0.3585422406	-0.5555491722	0.5724909946	-0.4280048536	0.2197901432	-0.0563375345	-0.0103252426	0.0050089378	0.0126142910	-0.0102975738
23	51.032	50.820	0.3686313576	-0.5654527299	0.5726638342	-0.4159212049	0.2025068956	-0.0443693649	-0.0123959303	0.0016174647	0.0146208643	-0.0095962763
24	54.440	54.264	0.3792527612	-0.5753188862	0.5719128145	-0.4027549597	0.1850662718	-0.0333847854	-0.0133271586	-0.0020313086	0.0161447311	-0.0085578541
25	57.931	57.793	-0.3903760680	0.5850703179	-0.5701813272	0.3885679874	-0.1676360901	0.0235006007	0.0131773165	0.0057914419	-0.0171378832	0.0072384763
26	61.421	61.405	0.4019696321	-0.5946293545	0.5674215611	-0.3734380233	0.1503889877	-0.0148159501	-0.0120257155	-0.0095219709	0.0175770381	-0.0057063461
27	65.080	65.099	-0.4140009176	0.6039189998	-0.5635955390	0.3574578295	-0.1334991990	0.0074102215	0.0099696929	0.0130919993	-0.0174642277	0.0040383838
28	68.696	68.875	-0.4264368134	0.6128638365	-0.5586759102	0.3407340429	-0.1171393576	0.0013416049	0.0071211407	0.0163852607	-0.0168261299	0.0023165600

Table 3. The same as Table 2, but for ^{226}Th.

L	Exp. [38]	Theo.	$\nu=0$	$\nu=1$	$\nu=2$	$\nu=3$	$\nu=4$	$\nu=5$	$\nu=6$	$\nu=7$	$\nu=8$	$\nu=9$
0	0	0	-0.2395120670	0.3559161264	-0.4168675898	0.4317728657	-0.4102009018	0.3615599332	-0.2946027497	0.2173350179	-0.1373294897	0.0622594713
1	3.191	0.337	-0.2347460754	0.3522489586	-0.4153924990	0.4323338587	-0.4121163322	0.3640157644	-0.2968752351	0.2189234152	-0.1380506017	0.0623199329
2	1	1	-0.2262173660	0.3455604256	-0.4126413509	0.4333082761	-0.4155812866	0.3684534943	-0.3009236226	0.2216482034	-0.1391441107	0.0622489320
3	4.259	1.967	-0.2155319442	0.3369686717	-0.4090277811	0.4345232447	-0.4200301774	0.3740978412	-0.3059144655	0.2247430537	-0.1400209454	0.0617285121
4	3.136	3.201	-0.2043223174	0.3277437296	-0.4051266748	0.4359075183	-0.4249209185	0.3801316652	-0.3109355854	0.2273599579	-0.1400380959	0.0604270161
5	6.24	4.663	-0.1937919498	0.3189566985	-0.4015237592	0.4375202995	-0.4298874664	0.3859160824	-0.3152376323	0.2287971408	-0.1386811965	0.0581045254
6	6.195	6.317	-0.1845829070	0.3112901985	-0.3986687729	0.4394873418	-0.4347571971	0.3910674987	-0.3183429784	0.2286099732	-0.1356527178	0.0546590166
7	9.112	8.136	-0.1769067195	0.3050641250	-0.3968269787	0.4419252052	-0.4394787392	0.3954027341	-0.3200098183	0.2265909499	-0.1308592842	0.0501156184
8	9.999	10.103	-0.1707306153	0.3003508937	-0.3961030571	0.4448988204	-0.4440445545	0.3988517281	-0.3201520984	0.2227043921	-0.1243628049	0.0445961692
9	12.785	12.206	-0.1659084369	0.2970776374	-0.3964835370	0.4484109497	-0.4484466992	0.4013989594	-0.3187790354	0.2170306955	-0.1163343955	0.0382888834
10	14.409	14.434	-0.1622588851	0.2951031893	-0.3978844733	0.4524149482	-0.4526603437	0.4030472496	-0.3159499487	0.2097209402	-0.1070134992	0.0314200313
11	17.152	16.779	0.1596031067	-0.2942633184	0.4001866849	-0.4568327131	0.4566442716	-0.4038039311	0.3117505220	-0.2009659091	0.0966751091	-0.0242295329
12	19.324	19.234	0.1577818511	-0.2943974213	0.4032614432	-0.4615724989	0.4603479756	-0.4036770906	0.3062768270	-0.1909714022	0.0856021786	-0.0169506972
13	22.105	21.793	-0.1566645815	0.2953570348	-0.4069911061	0.4665445850	-0.4637176702	0.4026697861	-0.2996210697	0.1799378660	-0.0740641712	0.0097957416
14	24.675	24.451	-0.1561518008	0.2970646830	-0.4112806056	0.4716703963	-0.4666993692	0.4007768897	-0.2918624359	0.1680473271	-0.0623040648	0.0029480798
15	27.554	27.205	-0.1561709405	0.2994124000	-0.4160587331	0.4768853849	-0.4692422894	0.3979857329	-0.2830633124	0.1554575712	-0.0505333259	-0.0034395301
16	30.413	30.053	-0.1566752713	0.3023631518	-0.4212804209	0.4821393766	-0.4712952542	0.3942708562	-0.2732659605	0.1423010674	-0.0389330870	-0.0092424746
17	33.418	32.994	-0.1576387716	0.3058952543	-0.4269217619	0.4873926502	-0.4728044852	0.3895947381	-0.2624953576	0.1286899267	-0.0276600065	-0.0143595883
18	36.497	36.029	-0.1590503593	0.3100049881	-0.4329730238	0.4926112280	-0.4737128258	0.3839092797	-0.2507642554	0.1147235416	-0.0168538790	-0.0187082043
19	39.627	39.16	-0.1609106851	0.3147020939	-0.4394332374	0.4977612698	-0.4739559244	0.3771580279	-0.2380805277	0.1004980382	-0.0066453337	-0.0222202960
20	42.896	42.387	-0.1632277474	0.3200033587	-0.4463035656	0.5028044624	-0.4734615174	0.3692805926	-0.2244557872	0.0861154723	0.0028383058	-0.0248406398

References

[1] A. Bohr, B.R. Mottelson, *Nuclear Structure, vol. II*, (Benjamin, New York) (1975).

[2] S.G. Rohozinski, Rep. Prog. Phys. **51**, 541 (1988)

[3] I. Ahmad, P.A. Butler, Annu. Rev. Nucl. Part. Sci. **43**, 71 (1993)

[4] P.A. Butler, W. Nazarewicz, Rev. Mod. Phys. **68**, 349 (1996)

[5] D. Bonatsos, D. Lenis, N. Minkov, D. Petrellis, P. Yotov, Phys. Rev. C **71**, 064309 (2005)

[6] D. Bonatsos, A. Martinou, N. Minkov, S. Karampagia, D. Petrellis, Phys. Rev. C **91**, 054315 (2015)

[7] R. Budaca, A. I. Budaca, and P. Buganu, Phys. Scr. **99**, 035309 (2024)

[8] M. Chabab, A. El Batoul, L. El Ouaourti, Nucl. Phys. A **1043**, 122818 (2024)

[9] W. Nazarewicz, P. Olanders, I. Ragnarsson, J. Dudek, G. A. Leander, P. Moller, and E. Ruchowska, Nucl. Phys. A **429**, 269 (1984)

[10] W. Nazarewicz and P. Olanders, Nucl. Phys. A **441**, 420 (1985)

[11] R. K. Sheline, Phys. Lett. B **197**, 500 (1987)

[12] J. Engel and F. Iachello, Phys. Rev. Lett. **54**, 1126 (1985)

[13] J. Engel and F. Iachello, Nucl. Phys. A **472**, 61 (1987)

[14] A. Boehnlein, M. Diefenthaler, N. Sato, M. Schram, V. Ziegler, C. Fanelli, M. Hjorth-Jensen, T. Horn, M. P. Kuchera, D. Lee, W. Nazarewicz, P. Ostroumov, K. Orginos, A. Poon, X.-N. Wang, A. Scheinker, M. S. Smith, and L.-G. Pang, Rev. Mod. Phys. **94**, 031003 (2022)

[15] R. Utama, J. Piekarewicz, and H. B. Prosper, Phys. Rev. C **93**, 014311 (2016)

[16] Z. M. Niu and H. Z. Liang, Phys. Lett. B **778**, 48 (2018)

[17] L. Neufcourt, Y. Cao, W. Nazarewicz, and F. Viens, Phys. Rev. C **98**, 034318 (2018)

[18] Z. M. Niu and H. Z. Liang, Phys. Rev. C **106**, L021303 (2022)

[19] X. H. Wu, Y. Y. Lu, and P. W. Zhao, Phys. Lett. B **834**, 137394 (2022)

[20] R. Utama, W.-C. Chen, and J. Piekarewicz, J. Phys. G: Nucl. Part. Phys. **43**, 114002 (2016)

[21] D. Wu, C. L. Bai, H. Sagawa, and H. Q. Zhang, Phys. Rev. C **102**, 054323 (2020)

[22] X.-X. Dong, R. An, J.-X. Lu, and L.-S. Geng, Phys. Rev. C **105**, 014308 (2022)

[23] N. J. Costiris, E. Mavrommatis, K. A. Gernoth, and J. W. Clark, Phys. Rev. C **80**, 044332 (2009)

[24] Z. M. Niu, H. Z. Liang, B. H. Sun, W. H. Long, and Y. F. Niu, Phys. Rev. C **99**, 064307 (2019)

[25] Z.-A. wang, J. Pei, Y. Liu, and Y. Qiang, Phys. Rev. Lett. **123**, 122501 (2019)

[26] R.-D. Lasseri, D. Regnier, J.-P. Ebran, and A. Penon, Phys. Rev. Lett. **124**, 162502 (2020)

[27] Z.-X. Yang, X.-H. Fan, T. Naito, Z.-M. Niu, Z.-P. Li, and H. Liang, arXiv: 2205.15649 (2022).

[28] X. H. Wu, Z. X. Ren, and P. W. Zhao, Phys. Rev. C **105**, L031303 (2022)

[29] R. D. Woods and D. S. Saxon, Phys. Rev. **95**, 577 (1954)

[30] M. Çapak, D. Petrellis, B. Gönül and Dennis Bonatsos, J. Phys. G: Nucl. Part. Phys. **42**, 095102 (2015)

[31] A. Ya. Dzyublik and V. Yu. Denisov, *Yad. Fiz.* **56** 30 (1993),[*Phys. At. Nucl.* **56** 303 (1993).]

[32] V. Yu. Denisov and A. Ya. Dzyublik, Nucl. Phys. A **589**, 17 (1995)

[33] D. Lenis, D. Bonatsos, Phys. Lett. B **633**, 474 (2006)

[34] S.G. Nilsson, Mat. Fys. Medd. K. Dan. Vidensk. Selsk. **29**(16), 1 (1955)

[35] H. Sobhani, H. Hassanabadi and D. Bonatsos, Eur. Phys. J. Plus **136**, 398 (2021)

[36] D. Bonatsos, H. Sobhani, H. Hassanabadi, Eur. Phys. J. Plus **135**, 710 (2020)

[37] G.B. Arfken, H.J. Weber, F.E. and Harris, *Mathematical Methods for Physicists: A Comprehensive Guide* (Elsevier Science) (2013).

[38] https://www.nndc.bnl.gov/nudat3/

[39] A. Geron, *Hands-On Machine Learning with Scikit-Learn, Keras, and TensorFlow: Concepts, Tools, and Techniques to Build Intelligent Systems*. 2nd Edition, (O'Reilly Media, Inc., Sebastopol) (2019).

[40] A. R. Edmonds, *Angular Momentum in Quantum Mechanics* (Princeton University Press, Princeton) (1957).